RSC Advances

PAPER

View Article Online
View Journal | View Issue

Cite this: *RSC Adv.*, 2022, **12**, 5012

The impact of fluence dependent proton ion irradiation on the structural and optical properties of $Bi_5In_{30}Se_{65}$ thin films for nonlinear optical devices

P. Priyadarshini,[a] S. Das,[a] D. Alagarasan,[b] R. Ganesan,[b] S. Varadharajaperumal,[c] S. Sahoo[de] and R. Naik *[a]

Received 6th January 2022
Accepted 25th January 2022

DOI: 10.1039/d2ra00097k

rsc.li/rsc-advances

This paper reports the effects of ion irradiation on the structural, linear, and nonlinear optical properties of thermally evaporated $Bi_5In_{30}Se_{65}$ thin films. The prepared films were irradiated with 30 keV proton ions with different fluences, such as 5×10^{15} ions per cm^2, 1×10^{16} ions per cm^2, and 5×10^{16} ions per cm^2. Structural analysis *via* X-ray diffraction (XRD) confirmed the non-crystalline nature of the film after ion irradiation with different doses. However, after the irradiation dose, the surface morphology changed, as shown by atomic force microscopy (AFM) images and field emission scanning electron microscopy (FESEM) images. The compositions of the films were obtained using energy-dispersive X-ray spectroscopy (EDX). Optical analysis *via* UV-Visible spectroscopy showed a reduction in the transmittance and an increase in the absorption in the higher wavelength region with irradiation. The optical bandgap and Tauc parameter decreased with an increase in the irradiation fluence, which is due to an increase in the irradiation-induced defects and disorder inside the system. The increases in the third order nonlinear susceptibility and the nonlinear refractive index with ion fluence are useful for nonlinear optical applications. The linear refractive index calculated from the transmittance data increased, satisfying Moss's rule. The optical parameters, such as lattice dielectric constant, optical density, skin depth, optical conductivity, real and imaginary dielectric constants, optical conductivity, loss factor, VELF, and SELF, were calculated using several empirical relationships and showed increasing behavior with the ion irradiation dose. The changes obtained in both the linear and nonlinear parameters will be useful for nonlinear optical device applications.

1. Introduction

Nowadays, the response of materials to intense external energy inputs such as thermal annealing,[1,2] laser irradiation,[3,4] ion irradiation,[5,6] and doping[7,8] to achieve the desired characteristics for fundamental studies and technological applications is gaining much attention. Among them, ion irradiation is one of the distinctive external energy input techniques that improve the structural and optical properties together with modification of the microstructural patterns of the system. These modifications are helpful when precisely designing the material properties required for the desired device applications. Several studies based on the consequences of the effects of ion irradiation have been carried out previously. The different doses of ion irradiation in $Ge_{23}Se_{62}As_{15}$ thin films showed modifications of the surface morphology and optical properties which are useful for telecom and sensing applications.[9] The ion implantation in Bi/$GeSe_2$ films induces a significant alteration in the optical bandgap with the appearance of a topological Bi_2Se_3 phase in the structure.[10] The proton irradiation of a Bi_2Te_3 film successfully enhances the defects' content, thus, enhancing the thermoelectric properties.[11] These fascinating results from ion irradiation on various material characteristics have motivated the study of the ion irradiation impact on the films reported here.

According to the energy transmitted through materials, the ion beams are divided into two categories such as low energy and high energy ion beams. The high energy ion beams possess energy ranging from a few tens of MeV to GeV that are carried by high atomic mass ions through inelastic collisions. The energetic ion beams with energy ranging from a few tens of keV to hundreds of keV are considered as low energy ion beams,

---

[a] Department of Engineering and Material Physics, ICT-IOC, Bhubaneswar, 751013, India. E-mail: ramakanta.naik@gmail.com

[b] Department of Physics, Indian Institute of Science, Bangalore, 560012, India

[c] Centre for Nano Science and Engineering, Indian Institute of Science, Bangalore-560012, India

[d] Laboratory for Low Dimensional Materials, Institute of Physics, Bhubaneswar 751005, India

[e] Homi Bhabha Training School Complex, Anushakti Nagar, Mumbai 400094, India

generate defects and disorder in the system.[12] Low energy ion beams basically interact with the target at the atomic level. After the bombardments of the target material, the accelerating incident ions experience a number of nuclear and electronic collisions. As a consequence of these elastic collisions, the ions lose all their energy and are implanted inside the target materials, thereby modifying several properties.[13] Due to the elastic collisions, nuclear energy loss is more than electronic energy loss, and is mainly responsible for the material modification.[14]

In this regard, the Bi–In–Se films were considered the prototypical semiconducting materials with many useful applications. The high glass-forming ability of selenium and the presence of indium give the alloy photovoltaic properties, softness, and easy fusibility, and suitability for application purposes.[15] After that, the addition of bismuth results in a considerable variation in linear and nonlinear optical properties as well as the structural phenomenon of the host system, in addition to carrier type reversal (CTR).[16,17] For example, in addition to the CTR, the Bi doping also showed a large variation in the linear and nonlinear optical properties in the $Bi_xIn_{25-x}Se_{75}$ thin films.[18] The replacement of indium with bismuth provides a constant coordination number ($Z = 2.25$) that represented the structure in the floppy state which helps to determine the modifications in the network topology apart from the CTR behavior of the Bi–In–Se system.[18,19] The modifications of several properties by varying the bismuth concentration in the $Bi_xIn_{35-x}Se_{65}$ films results in the crystallinity of the highly Bi-doped films with a decrease in the optical bandgap.[20] Until now there has been no relevant research on the impact of ion irradiation on Bi–In–Se thin films. So, in this study, we were interested in determining the outcome of the irradiation of low energy carried light ions, such as protons, on the Bi–In–Se thin film. Previously, the $Bi_5In_{30}Se_{65}$ thin-film gained much attention because it showed the highest transmittance out of all the other $Bi_xIn_{35-x}Se_{65}$ films, as well as showing an abrupt change in various linear and nonlinear optical parameters. Thus, in the present research, we were interested in studying the impact of ion irradiation on various structural, morphological, and optical linear and nonlinear properties of the $Bi_5In_{30}Se_{65}$ thin-film with different fluences. Several studies have been performed on ion irradiation to demonstrate the tailoring of various characteristics of materials. For example, the effect of 80 MeV silicon swift heavy ion irradiation on the linear and nonlinear properties of the $Ge_{24}Se_{61}Sb_{15}$ films makes them suitable for use in telecommunication and sensing applications.[21] The ion irradiation, induced changes in the DC conductivity, and the electrical transport of the $Ge_{20}Se_{80-x}Bi_x$ films which is associated with the electronic energy loss of the ions inside the target material.[22] With As–Se–Bi thin films, the use of 120 MeV Ag swift heavy ion irradiation, induced a decrease in the bandgap, and an increase in conductivity together with a p to n transition.[23] The 3 MeV proton irradiation decreased the bandgap and increased the refractive index, dispersion energy in the amorphous-$(Ge_{20}Se_{80})_{0.96}Ag_{0.04}$ thin films due to structural modification.[24] The proton and deuteron irradiation changed the electronic conductivity under the influence of irradiation parameters and there was no change in the ionic conductivity of the quaternary Ag–Ge–As–S composite materials.[25] The influence of proton beam irradiation over a $Ge_{40}Se_{60}$/Ag film stack reveals silver surface deposition and germanium oxidation, and a change in the film's chemistry as a result of proton irradiation.[26] The electrical resistivity decreased with 10 MeV proton irradiation fluence in Cu(In,Ga)Se_2 thin films which is due to the reduction of the concentration of the compensating donor-like defects, specifically the selenium vacancies.[27]

So, in the present study, the focus was on the proton irradiation-induced modifications in the structural, morphological, and optical properties of thermally evaporated $Bi_5In_{30}Se_{65}$ thin films caused by different irradiation fluences. Because there was no previous significant research findings on the effect of ion implantation on the Bi–In–Se thin films, so as a first attempt, we were interested to expose the thin film to be irradiated by low energy proton ions with different fluences, which were precisely chosen to achieve a controllable performance. Thus, the change in properties was investigated at three different proton ion fluences: 5×10^{15} ions per cm^2, 1×10^{16} ions per cm^2, and 5×10^{16} ions per cm^2 with low energy protons (30 keV) on $Bi_5In_{30}Se_{65}$ thin films. The X-ray diffraction method (XRD) and atomic force microscope (AFM) were used to investigate the proton irradiation-induced structural alteration. The compositional analysis and surface morphological structure of the irradiated films were observed using energy-dispersive X-ray spectroscopy (EDX) attached to a field emission scanning electron microscope (FESEM). The UV-Vis spectroscopy was used for the optical study over the wavelength range of 450–1100 nm.

2. Experimental procedure

2.1 Sample preparation

The bulk glassy of highly pure $Bi_5In_{30}Se_{65}$ was synthesized using the universal melt quenching procedure. Stoichiometric amounts of the high-purity elements Bi, In, and Se (99.999% Sigma-Aldrich) were weighed using an accurate sensitive balance, and then mixed inside a clean quartz ampoule evacuated under a pressure of 10^{-3} Torr. Then the ampoules were maintained in a high-temperature gradient at a heating rate of about 3–4 °C min^{-1} until 500 °C was reached inside the furnace and then that temperature was held for 20 h. These ampoules were frequently oscillated inside the furnace to confirm that the homogeneity of the molten mass had been obtained. Subsequently, the ampoules were taken out of the furnace and rapidly quenched in ice-cold water to avoid crystallinity. After that, the ampoules were broken and the bulk alloy was collected, and ground to give the powdered form.

The homogeneous $Bi_5In_{30}Se_{65}$ thin films of ~800 nm thickness were achieved using the thermal evaporation method. To avoid air contamination inside the chamber, a vacuum coating unit (Hind-HiVac, Model 12A4D) was employed to create a vacuum atmosphere under 10^{-5} Torr pressure. Subsequently, a controllable deposition rate of 0.5 nm s^{-1} was maintained, whilst the $Bi_5In_{30}Se_{65}$ chalcogenide vapor was deposited onto a cleaned glass substrate. Meanwhile, the deposition rate was monitored using a quartz crystal monitor. The substrate holder was rotated continuously to form a uniform and homogeneous film.

The prepared thin films were irradiated with 30 keV proton irradiation using a low energy ion implanter at Institute of Physics (IOP, Bhubaneswar, India). The proton irradiation was performed at three different fluences: 5×10^{15} ions per cm^2, 1×10^{16} ions per cm^2, and 5×10^{16} ions per cm^2 under a high vacuum atmosphere ($\sim 10^{-11}$ Torr) in the chamber. The ions were incident perpendicular to the sample surface. The desired ions (proton ions) were directed towards the sample by providing a certain voltage and current through a magnetic field. The ion beam was magnetically scanned over a 1 cm × 1 cm area covering the complete thin film surface that was fixed on a target ladder for uniform implantation and loaded inside the irradiation chamber. The ladder has the advantage of being able moving up and down which is controlled by a knob. The precisely controlled fluences and beam current were chosen by considering the time period and number of counts of the course of irradiation:

$$\text{Time period} = \frac{\text{fluence} \times \text{exposed area}}{\text{beam current (nA)}}$$

$$\text{Number of counts} = \frac{\text{fluence} \times \text{area} \times \text{charge of ion} \times 1.6 \times 10^{-19}}{\text{scale of current integrator}}$$

2.2 Sample characterization

The structural characterizations of the proton irradiated $Bi_5In_{30}Se_{65}$ film with different fluences were carried out by XRD (Bruker, D8 Advance) with a Cu K_α line ($\lambda = 1.54$ Å). The scanning range was 5°–80° at step size of 0.05° s^{-1} with a grazing angle of 1°. The irradiation induced topographic changes were investigated by AFM (APE Research, A-100). The modification in the elemental composition and surface morphological structure of the films due to irradiation was observed using a EDX spectrometer attached to an FESEM unit (Carl Zeiss, Ultra 55). The optical transmission data of the films were recorded by using a UV-Visible spectrophotometer (Syntronics, India, AU2702 over a 450–1100 nm range). The linear optical parameters, such as absorption coefficient (α), extinction coefficient (k), optical density (OD), and refractive index (n) were evaluated using the transmittance data. Likewise, the optical bandgap (E_g), and Tauc parameters ($B^{1/2}$) were calculated from the Tauc relationship. The Dimirov and Sakka empirical relationship, and Miller's rule were implemented for the calculation of the static refractive index (n_0), high-frequency dielectric constant (ε_∞), and nonlinear parameters such as nonlinear susceptibility ($\chi^{(3)}$) and nonlinear refractive index (n_2).

3. Results and discussion

3.1 Structural analysis

3.1.1 Energy loss process. The electronic and nuclear energy losses to the films during the ion irradiation resulted in modifications to some of their properties. Therefore, here the energy loss of the 30 keV proton ions in the Bi–In–Se target was calculated using SRIM-2008 software. The ion range (R_p) and the energy losses (S_e and S_n), and the longitudinal and lateral straggling of the 30 keV proton ion in the Bi–In–Se film are given in Table 1.

In Fig. 1(a), the electronic energy loss (S_e) and the nuclear energy loss (S_n) are shown as a function of energy. The figure shows that the electronic energy loss is dominant over nuclear energy loss which agrees with results of other studies.[28,29] The dominating nature of the S_e indicates that the energy loss may ionize the target atoms, or excite the electrons of the target from the valence band (VB) to the conduction band (CB), or may result in a plasmonic effect which results in the alteration of several properties. The range of ions (274.4 nm) is within the range of the $Bi_5In_{30}Se_{65}$ film thickness (~800 nm). Thus, the ions easily penetrate through the film and become implanted in the thin films.

3.1.2 XRD analysis. The XRD patterns of the proton irradiated $Bi_5In_{30}Se_{65}$ films irradiated at 5×10^{15} ions per cm^2, 1×10^{16} ions per cm^2, and 5×10^{16} ions per cm^2 fluence are shown in the Fig. 1(b). The absence of any sharp peaks and the presence of broad humps implied that the films retain an amorphous nature under proton irradiation like the as-prepared form in a previous study by Priyadarshini *et al.*[20]

3.1.3 AFM analysis. The ion irradiation induced a surface morphological change that was noticed from the 5 µm × 5 µm three-dimensional AFM images (Fig. 2). The RMS roughness for 5×10^{15}, 1×10^{16}, and 5×10^{16} ions per cm^2 fluence films are found to be 13.58 nm, 1.44 nm, and 2.12 nm, respectively. Different roughnesses after irradiation indicated that the projectile ions possessed sufficient energy to induce surface modification and create disorders inside the material. The change in the film surface structure is clearly visible from the AFM image.

3.1.4 FESEM and EDX analyses. The element concentration analysis was performed using the EDX measurements which confirmed the presence of corresponding elements such as: Bi, Se and In in the different proton irradiated films. The inset Fig. 3 shows the presence of elements for the $Bi_5In_{30}Se_{65}$ proton irradiated films at different fluences. The composition obtained

Table 1 The range and the energy loss of a 30 keV proton ion in Bi–In–Se films

Sample	S_e (keV nm^{-1})	S_n (keV nm^{-1})	Range (nm)	Longitudinal straggling (nm)	Lateral straggling (nm)
Bi–In–Se	0.08693	0.00044	274.4	140.1	123.8

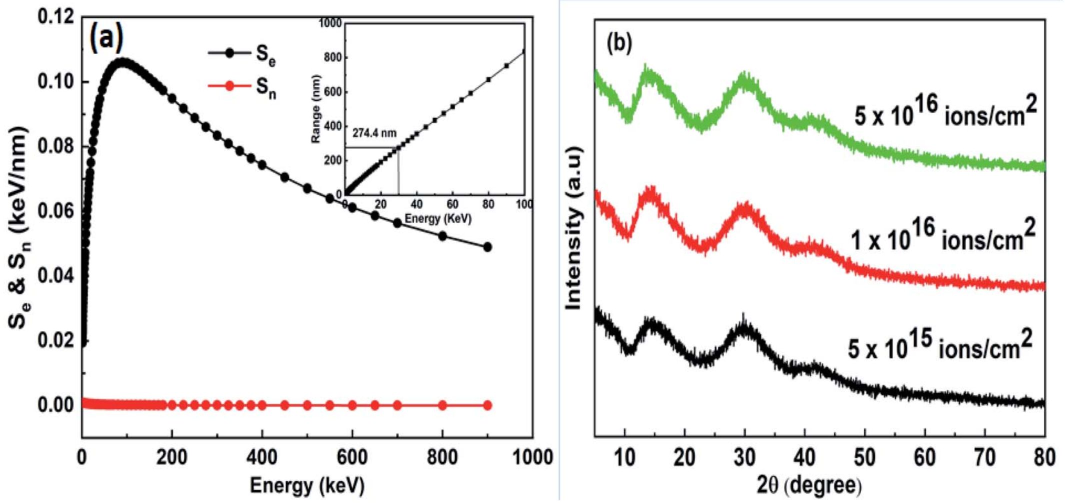

Fig. 1 (a) The SRIM simulation of S_e S_n and the range (inset), and the (b) XRD patterns of 30 keV proton ion irradiated $Bi_5In_{30}Se_{65}$ films at different fluences.

from the EDX analysis is given in Table 2. The different peaks correspond to the respective elements and the composition of the different films were nearly the same and were within 3% error from the calculated value.

The FESEM images at the scale of 100 nm are shown in Fig. 3, which clearly show the homogeneity and uniformity of the studied films. The 5×10^{16} ion irradiated film shows some granular structure which might be due to the ion irradiation. The films studied were of 1×1 cm^2 shape with a film thickness of ~800 nm deposited on a glass substrate. We have calculated the particle sizes for all irradiated films were calculated using ImageJ software (Java 1.8.0_172 version) and this software was

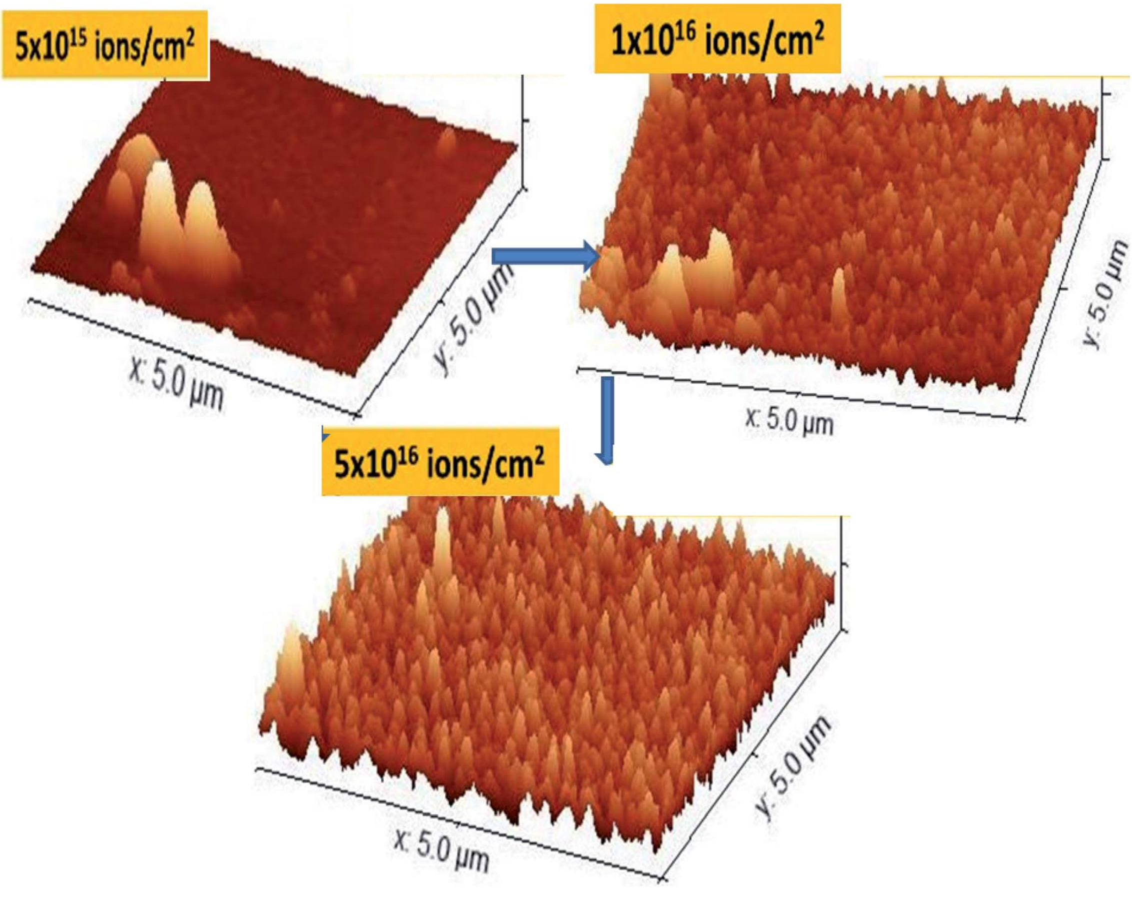

Fig. 2 AFM images of the ion irradiated $Bi_5In_{30}Se_{65}$ thin films.

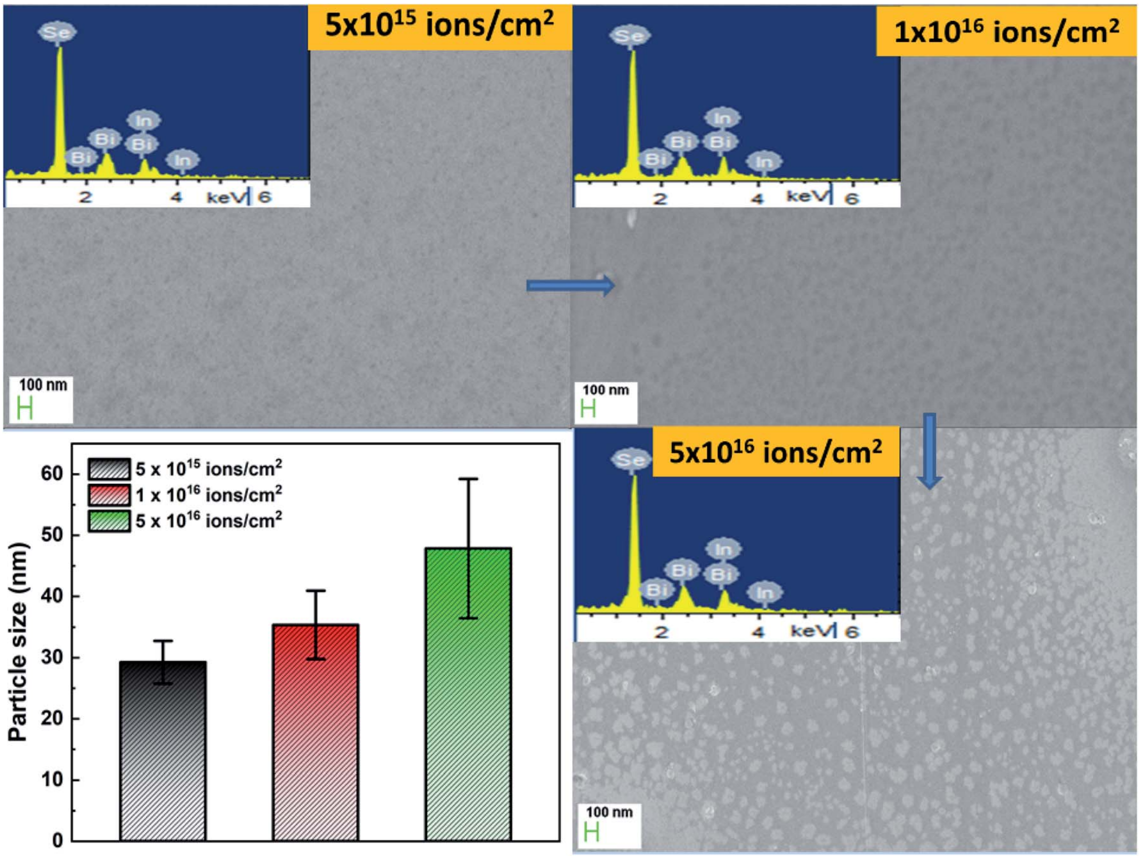

Fig. 3 FESEM and EDX images and a particle size histogram of the ion irradiated $Bi_5In_{30}Se_{65}$ thin films.

also used for the statistical analysis shown in Fig. 3. The observed particle sizes were in range of 29.26 nm (5×10^{15} ions per cm^2), 35.34 nm (1×10^{16} ions per cm^2), 47.82 nm (5×10^{16} ions per cm^2). It was observed that the particle size was enhanced with an increase in the ion irradiation dose which was also clearly seen from the FESEM image. However, there was no sign of any crystallinity from the XRD data. This enhancement in the particle size indicated that irradiation led to an enhancement of the concentration of large particles, and the disappearance of smaller particles with the formation of a granular structure. The results of the FESEM analysis confirmed that the grains covered the entire surface of the substrate. The appearance of a larger particle size will improve the performance of the solar cell, as the charge carriers encounter fewer trapping and scattering sources.[30]

3.2 Optical analysis

3.2.1 Linear optical properties

Transmittance (T) and reflectance (R). The optical properties of the material deal with the various phenomenon of light interactions with the material and the related modifications of the material's behavior. Thus, those properties are closely related to the material's atomic structure, electronic band structure, and electric properties. The optical behavior plays an important role in determining the applicability of the for use in optoelectronic devices.[31,32] The optical transmittance (*T*) and reflectance (*R*) of

Table 2 Composition of the proton irradiated $Bi_5In_{30}Se_{65}$ thin films at different fluences

	$Bi_5In_{30}Se_{65}$			
Sample	5×10^{15} ions per cm^2		1×10^{16} ions per cm^2	5×10^{16} ions per cm^2
Element	Calc. (at%)	Obs. (at%)	Obs. (at%)	Obs. (at%)
Se	65	66.85	66.30	67.03
In	30	29.10	28.97	28.62
Bi	5	4.05	4.73	4.35
Total	100	100	100	100

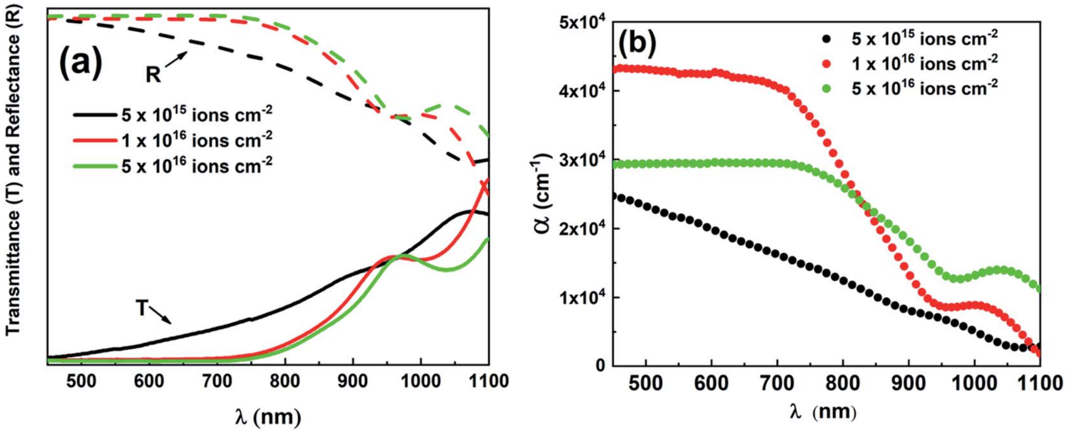

Fig. 4 (a) The transmittance and reflectance, and (b) the absorption coefficients of the studied thin films.

different ion irradiated Bi–In–Se films are shown in Fig. 4(a) for the wavelength range of 450–1100 nm. The transmittance spectrum consisted of few numbers of distinct fringes over the visible to infrared region. The appearance of the fringes was caused by the interference phenomenon between light, the substrate, and the film interface medium.[33] It was observed that the transmittance decreased with an increase in the ion irradiation fluence. This reduction in the transmittance behavior of the irradiated film was due to an increase in lattice defects and the creation of localized states within the VB and the CB.[34] The absorption edge shifted to a higher wavelength region with an increase in the fluence.

Absorption coefficient (α). The absorption coefficient (α) of the irradiated $Bi_5In_{20}Se_{65}$ thin film was determined from the transmittance $T(\lambda)$ and film thickness (d) by following formula:[35]

$$\alpha = \frac{1}{d}\ln\frac{1}{T} \quad (1)$$

Fig. 4(b) shows the spectral dependence of the absorption coefficient on the wavelength for the irradiated films. It was observed that the absorption coefficient decreased as the wavelength increased and in addition it also increased with the ion irradiation dose. The films possessed a large absorption coefficient of 10^4 cm^{-1} over the visible range which was in agreement with research reported in the literature.[8,36]

Extinction coefficient (k), optical bandgap (E_g), and Tauc parameter ($B^{1/2}$). The extinction coefficient (k) or absorption index played an important role in the determination of several optical measurements which were related to the absorption of light waves in the medium, and the dielectric constants. This was related to the fraction of light that was scattered or absorbed over unit distance through the medium. The extinction coefficient k values were estimated by the formula:[37] $k = \frac{\alpha\lambda}{4\pi}$. Fig. 5(a) shows the extinction coefficient as a function of incident energy for the proton irradiated thin films. The extinction coefficient primarily increased with energy, and then decreased with a higher energy value, which indicated that the film became more transparent at a higher energy. The lower value of k over a higher energy region represented the loss of light by scattering and absorption, whereas the propagation was

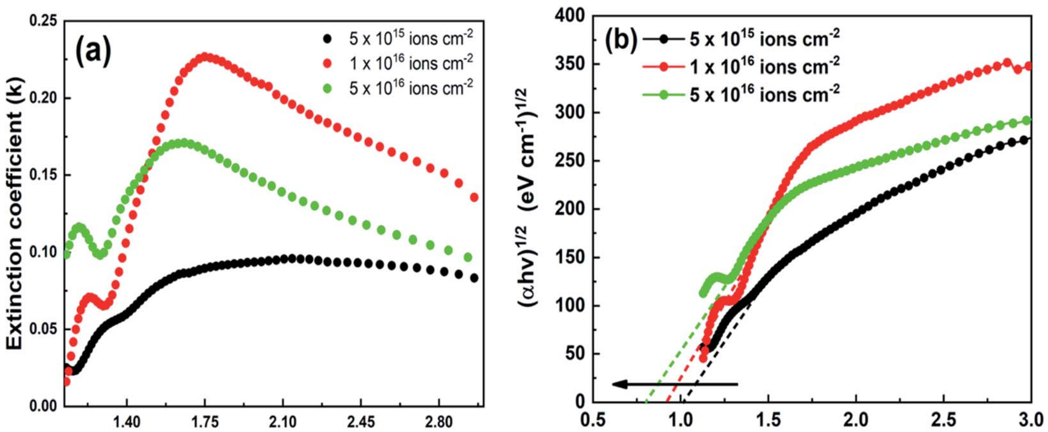

Fig. 5 (a) Variation in extinction coefficient values and (b) $(\alpha h\nu)^{1/2}$ *vs.* $h\nu$ plots of the proton irradiated thin films.

decreased in the films studied. From this figure, it can be observed that the extinction coefficient k varies with the ion irradiation dose.

The effective bandgap of the films studied was calculated from the Tauc relationship[38] as given by:

$$(\alpha h\nu) = B(h\nu - E_g)^p \tag{2}$$

where B is the Tauc parameter which describes the degree of disorder in the materials, ν is the frequency of the incident beam, E_g is the optical bandgap, p (exponent) is related to the nature of various electronic transitions in a particular range. The value of p has different values such as 1/2, 2, 3/2, and 3 depending on the different types of transition such as: direct allowed, indirect allowed, direct forbidden, and indirect forbidden, respectively.[39] According to Tauc, the amorphous materials possessed an indirect allowed bandgap. In this study the as-prepared and irradiated films retain their amorphous nature, and thus they are considered to be an indirect allowed transition ($p = 2$). The extrapolation of the straight-line portion of the $(\alpha h\nu)^{1/2}$ *vs.* photon energy ($h\nu$) in Fig. 5(b) gave the following E_g values of the corresponding films: 1.01 eV (5×10^{15} fluence), 0.92 eV (1×10^{16} fluence), 0.79 eV (5×10^{16} fluence), which were in agreement with the results given in other studies.[8,40] The reduction in E_g was due to the increase in localized states over the mobility gap. According to the Mott and Davis model,[41] the degree of disorder, and the defects created by unsaturated and dangling bonds increased the width of the localized states. These localized states near the bandgap edge caused an increase in the carrier concentration. Thus, the increase in the carrier concentration as a consequence of ion irradiation reduced the bandgap values.[42] The low energy proton irradiation resulted in a number of collisions between the proton ion and the inner material ions, which resulted in the creation of disorders and defects. Therefore, these defects and disorders affected the band tailing and reduced the optical bandgap of the materials.[7] The slope of eqn (2), represents the degree of disorder, which had decreased from 333 $\text{cm}^{-1/2}\,\text{eV}^{-1/2}$ (5×10^{15} fluence) to 264 $\text{cm}^{-1/2}\,\text{eV}^{-1/2}$ (5×10^{16} fluence) with an increase in the fluence. This decrease showed the increase in the degree of disorder as the Tauc parameter varied inversely with the disorder. The observed behavior can be useful for several optoelectronic device applications. For example, organic–inorganic-based single polyaniline nanowire doped quantum dots showed a high responsivity (such as absorbance and photoluminescence (PL)) over the wavelength range of 350 nm to 700 nm. This high response over the wavelength range was mainly due to the high density of localized states (trapping states) that reduced the recombination rate and increased the light detection. Thereby such behavior with a tunable spectral variation makes them suitable for photodetection applications.[43] In this case, the absorption edge of the films studied occurred at ~650–850 nm and showed a reduced pattern for the optical band gap (from 1.01 eV to 0.79 eV) which was also due to the enhancement of the localized state concentration over the bandgap region. Thus, the $Bi_5In_{30}Se_{65}$ thin film may be a possible candidate for use in broadband photodetector applications.

Using an organic poly(vinylpyrrolidone) (PVP) matrix doped with MoS_2, quantum dots organic–inorganic hybrid nano-waveguides were developed, and then these were used as guides to obtain combined subwavelength field localization. Two different colors of light emissions at the nano-waveguide terminals were achieved due to self-absorption-related energy dissipation. The work was based on the organic PVP matrix doped with MoS_2 quantum dots waveguide which showed the variation in PL intensity evolution, which occurred as the ~575 nm shifted to 580 nm as the distance increased. This uniform and stable colorful emission could possibly be used in applications including optical routing in photonic circuits and devices, colorful displays, and output coupling of laser emissions.[44] Similarly, high-quality hexagonal Cu_2Te microdisks on copper foam were fabricated using chemical vapor deposition (CVD). This study showed PL at ~627.5 nm and an enhancement in charge transfer and exciton resonance in surface enhanced Raman spectroscopy (SERS) detection showed the potential for its use in light-emitting diodes, lasers, and so on.[45] As is already known, PL basically involves contributions from high-energy near band emission recombination and low-energy bands corresponding to deep level transitions (optical energy gap) and defects.[46] These factors are very much responsible for the shifting of the PL spectra towards higher/lower wavelengths. In this case, the decrease of optical bandgap (1.01–0.79 eV) with an increase in defect density, and red shifting of the absorption edge (650–850 nm) was nearly close to the referred PL peak positions. Hence, the irradiated $Bi_5In_{30}Se_{65}$ film may be a potential candidate for use as optical waveguides, red lasing, photonics, and biological detection of aromatic molecules, optical routing in photonic circuits and device applications.

Furthermore, the monolayer MoS_2 with a low dimensional nanostructure shows potential for use in practical light-emitting applications. Here, the recent advances on the manipulations done in monolayer MoS_2 by plasmonic nanostructures to obtain PL, and their possible applications in nanoscale photonics and optoelectronics are presented. The bandgap normalization of the MoS_2 monolayer showed a high bandgap (~2.19 eV) without photoexcitation, which was about 0.4 eV lower than that of the undoped MoS_2 monolayer, and which showed environmental stability, high optical transparency, and PL spectra at ~680 nm. These characteristics were also close to those of our irradiated films which showed optical transparency, a close absorption edge, and so on, meaning that the studied samples were useful for light generation, transmission, modulation, and detection applications.[47]

Refractive index (n), static refractive index (n_0), and high-frequency dielectric constant (ε_∞). The refractive index is considered as an essential optical parameter which plays an important role in designing optical devices, and also provides information on the local fields, polarization, and phase velocity of light in the propagating material. The corresponding absorption edge of the studied films occurred at 650–850 nm, thus the refractive index was calculated by using the transmittance obtained from the formula:[48,49]

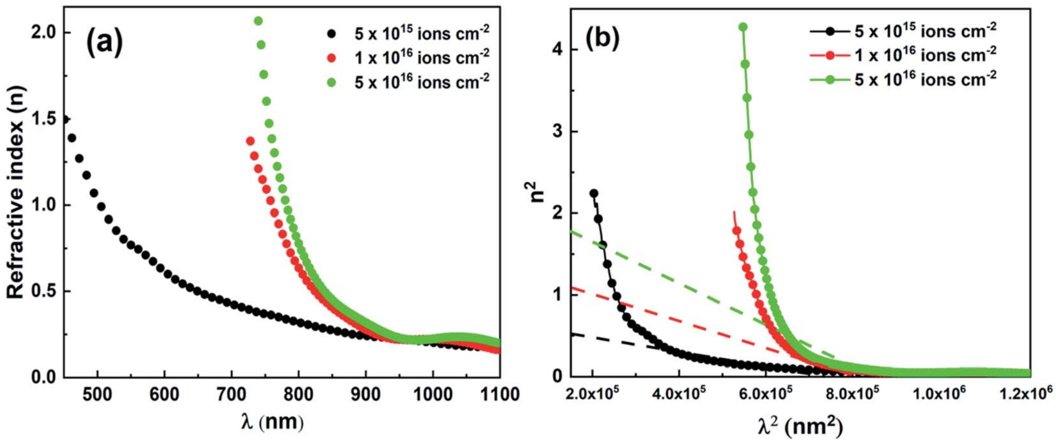

Fig. 6 (a) The increase in the refractive index with fluence and (b) n^2 *vs.* λ^2 plots used to evaluate N/m^* and ε_∞.

$$n = \frac{1}{T_s} + \left(\frac{1}{T_s - 1}\right)^{1/2} \tag{3}$$

where T_s is the percentage transmission coefficient. Fig. 6(a) shows the variation of the refractive index with wavelength which illustrates the increase of the refractive index with doses of irradiation. The refractive index shows normal dispersion behavior. The behavior of the refractive index satisfies Moss's rule[50] ($E_g n^4$ = constant) where the E_g showed inversely proportional behavior to the refractive index.[51,52]

The static linear refractive index and high-frequency dielectric constant, $\varepsilon_\infty = n_0^2$ of the different ion irradiated $Bi_5In_{30}Se_{65}$ films were calculated using the Dimitrov and Sakka relationship:[53]

$$\frac{n_0^2 - 1}{n_0^2 + 2} = 1 - \sqrt{\frac{E_g}{20}} \tag{4}$$

where E_g corresponds to the optical bandgap estimated by the Tauc relationship. The obtained values of static refractive index and high-frequency dielectric constant are given in Table 3. It can be observed that both ε_∞, and n_0 increase as the irradiation dose increases.

High-frequency dielectric constant (ε_∞) and carrier concentration (N/m).* The high-frequency dielectric constant (ε_∞) and the ratio of carrier concentration per the effective mass (N/m^*) can be estimated as follows:[54]

$$n^2 = \varepsilon_1 = \varepsilon_\infty - \left(\frac{e^2}{4\pi^2 c^2 \varepsilon_0}\right)\left(\frac{N}{m^*}\right)\lambda^2 \tag{5}$$

where ε_∞ represents the high-frequency dielectric constant, e is the charge of an electron, N is the free charge carrier concentration, ε_0 is the permittivity of the free space, m^* is the effective mass of the free charge carriers and c is the velocity of light. Here, by extrapolation of the straight line obtained in Fig. 6(b), the N/m^* and ε_∞ were calculated from the slope obtained and the intersect of the linear portion of the plot. The values of N/m^* and ε_∞ obtained are listed in Table 3. It was observed that the carrier concentration and the high-frequency dielectric constant increased with the ion irradiation dose which was consistent with the refractive index behavior.

Plasma frequency (ω_p), optical density (OD), and skin depth (δ). According to the Drude model, the plasma frequency (ω_p) is a fundamental optical property which can be calculated by the formula:[55]

$$\omega_p^2 = \left(\frac{e^2}{\varepsilon_0 \varepsilon_\infty}\right)\frac{N}{m^*} \tag{6}$$

Table 3 Optical parameters of the irradiated $Bi_5In_{30}Se_{65}$ thin films

Optical parameter	5×10^{15} ions per cm^2	1×10^{16} ions per cm^2	5×10^{16} ions per cm^2
Optical bandgap (E_g) (eV)	1.01 ± 0.02	0.93 ± 0.01	0.79 ± 0.02
Tauc parameter ($B^{1/2}$) (cm$^{-1/2}$ eV$^{-1/2}$)	333 ± 3	321 ± 2	263 ± 2
Static linear refractive index (n_0)	3.36	3.45	3.61
High frequency dielectric constant of the lattice ($\varepsilon_\infty = n_0^2$)	11.34	11.91	13.09
Carrier concentration ($N/m^* \times 10^{39}$) (kg^{-1} m^{-3})	1.26	1.89	3.07
Dielectric constant of the lattice, ε_L (from n_2 *vs.* λ_2 plot)	0.69	1.35	2.15
Optical electronegativity (η_{Opt})	1.65	1.64	1.62
Plasma frequency ($\omega_p^2 \times 10^{12}$) (Hz)	1.30	1.00	1.03
First-order non-linear susceptibility ($\chi^{(1)}$)	0.82	0.86	0.96
Third-order non-linear susceptibility ($\chi^{(3)} \times 10^{-10}$ esu)	0.78	0.96	1.46
Non-linear refractive index ($n_2 \times 10^{-9}$ esu)	0.87	1.05	1.52

The estimated plasma frequency value for the films studied is presented in Table 3. The ω_p^2 value showed an increment from 1.306×10^{12} Hz to 1.008×10^{12} Hz with the increase in the ion irradiation dose and then it slightly decreased to 1.032×10^{12} Hz for the 5×10^{16} ion irradiated film. The change in the plasma frequency values indicated the change in the polarization process inside the system.[56]

The OD represents the measure of absorption loss of the incident radiation as it propagates through the materials. The OD can be estimated as,[4] OD $= \alpha \times d$. Fig. 7(a) shows the estimated OD values with wavelength (λ). The figure shows that the OD showed the same pattern as the absorption coefficient, *i.e.*, it increases with the ion irradiation doses. The absorbed energy in the material mostly depends on the extinction coefficient, type of material, and its conductivity and thickness over the absorption region. The absorbance percentage depends on the incident energy, which behaves exponentially when penetrating through the material system, which can be described by skin depth. Skin depth or penetration depth (δ) represents the path distance at which the incident radiation behaves exponentially with respect to the initial value. It is estimated from the reciprocal of the absorption coefficient (α),[57] *i.e.*, $\delta = 1/\alpha$. The skin depth variation with respect to energy ($h\nu$) is shown in Fig. 7(b). It was observed that the skin depth reduced to zero with an increase in energy. The height of these peaks was increased with the increase of the ion irradiation doses from 5×10^{15} ions per cm^2 to 1×10^{16} ions per cm^2 and then decreases with an ion irradiation dose of 5×10^{16} ions per cm^2.

Dielectric constants, loss factor, and quality factor. The dielectric constant is another important characteristic of the material that can be expressed as the real and imaginary dielectric constants. It basically relates the permittivity and polarizability of the material with the density of states within the forbidden energy gap region. The real part of the dielectric constant provides information about the slowdown of the speed of light when traversing through the material, whereas the respective imaginary part gives information about the absorption of energy by an electric field due to dipole motion. The values obtained for the refractive index and extinction coefficient have been used to evaluate the real (ε_r) and imaginary (ε_i) dielectric constants of the irradiated $Bi_5In_{30}Se_{65}$ thin films by the expressions:[58]

$$\varepsilon = \varepsilon_r + i\varepsilon_i = (n + ik)^2 \tag{7}$$

where, $\varepsilon_r = n^2 - k^2$ and $\varepsilon_i = 2nk$.

Fig. 8(a) and (b) show the wavelength dependence of the real and imaginary parts of the dielectric constant. It has been observed that both the estimated values, ε_i and ε_r increase with the ion irradiation dose. The imaginary dielectric constant had a lower value compared to the real dielectric constant which was mainly due to the low extinction coefficient values.

The dielectric loss factor represents the loss rate of the power dissipated by the motion of charges through the electromagnetic field. It basically depends on the real and imaginary dielectric constants and is defined as,[59] loss factor ($\tan\delta$) $= \varepsilon_i/\varepsilon_r$. Similarly, the reciprocal of the dissipation factor represents the quality factor given by quality factor $= 1/\tan\delta = \varepsilon_r/\varepsilon_i$.

The spectral variations of the loss factor and the quality factor are shown in Fig. 9(a) and (b). It can be seen that at a lower wavelength region, the dielectric loss tangent has a low value and then increases with the increase in wavelength. The increase in ion irradiation dose increases the energy losses. Similarly, the quality factor showed a reduction with wavelength and the corresponding peak slightly shifted to a higher wavelength with higher ion irradiation doses.

Volume and surface energy loss functions (VELF and SELF). When the energetic electrons pass throughout the thin film they lose energy due to the free electron density of the material. This characteristic energy loss is expressed by two parameters, *i.e.*, volume energy loss function and surface energy loss function, which can be calculated as follows:[60]

$$\text{VELF} = -\text{Im}\frac{1}{\varepsilon} = \frac{\varepsilon_i}{\varepsilon_r^2 + \varepsilon_i^2} \tag{8}$$

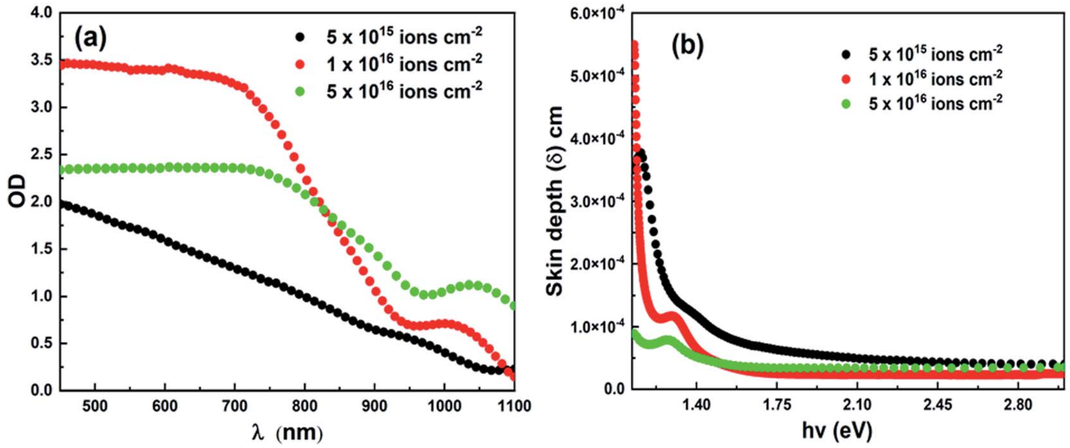

Fig. 7 (a) The optical density and (b) the skin depth variation of the thin films under different fluences.

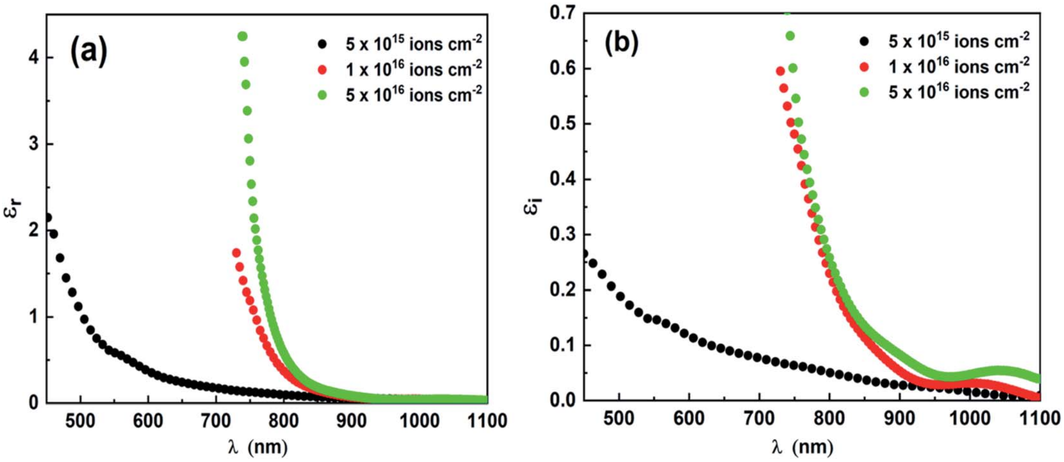

Fig. 8 (a) ε_r plots and (b) ε_i plots of the proton irradiated $Bi_5In_{30}Se_{65}$ thin films.

$$\mathrm{SELF} = -\mathrm{Im}\frac{1}{\varepsilon+1} = \frac{\varepsilon_i}{(\varepsilon_r+1)^2+{\varepsilon_i}^2} \tag{9}$$

Fig. 10(a) and (b) show the spectral dependence of VELF and SELF on the wavelength range of the irradiated thin films. It was observed that both SELF and VELF primarily increased with wavelength, and then decreased as the wavelength reached a higher value. The VELF was higher than SELF for the films studied in this research. This behavior was predictable in the case of semiconductor films, because the charge carriers suffer more collisions during the course of penetration through the bulk material. Also, increases in both VELF and SELF with ion irradiation doses could be due to an increase in defects and disorder which causes an increase in the collisions of the carrier during its journey through the material.[61]

Optical conductivity (σ). The optical conductivity in semiconductors showed an optical response with the incident light of the samples studied. This can be shown by the sum of real optical conductivity (σ_r) and imaginary optical conductivity (σ_i) that depended on the real and imaginary dielectric constants, given by:[62]

$$\sigma_{\mathrm{Opt}} = \sigma_r(\omega) + i\sigma_i(\omega), \tag{10}$$

where $\sigma_r(\omega) = \omega\varepsilon_0\varepsilon_i$ and $\sigma_i(\omega) = \omega\varepsilon_0\varepsilon_r$, where, ω represents angular frequency ($\omega = 2\pi v$), and ε0 is the electric permittivity of the vacuum. The spectral behavior of the real and imaginary optical conductivity with wavelength are shown in Fig. 11(a) and (b). From the plot, it can be observed that both σ_r and σ_i increased with an increase in the ion irradiation doses. The σ_i showed a larger value than σ_r. The red shifting of transmittance shows the decrease in the optical bandgap which was due to the increase of localized states over the gap region.[54] This decrease in the energy gap value increased the optical conductivity with the increased ion irradiation doses.

3.2.2 Nonlinear optical properties

Third-order nonlinear susceptibility ($\chi^{(3)}$) and nonlinear refractive index (n_2). The nonlinear optical parameters are very important in the field of optoelectronic applications. This

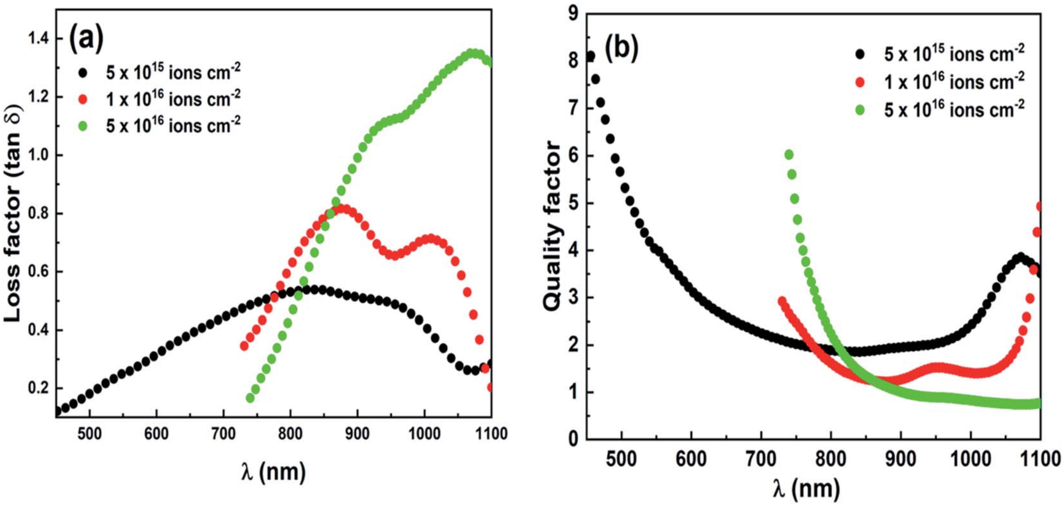

Fig. 9 (a) Loss factor and (b) quality factor plots of the proton irradiated $Bi_5In_{30}Se_{65}$ thin films.

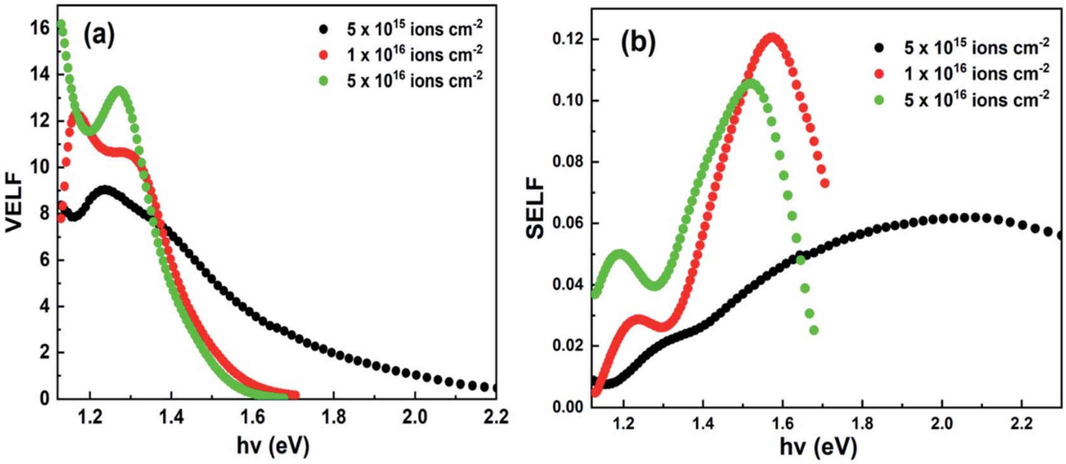

Fig. 10 (a) VELF and (b) SELF plots of the proton irradiated $Bi_5In_{30}Se_{65}$ thin films.

comes in to play when the intensity of incident radiation is sufficiently high that it can alter the properties of the materials. The linear optical susceptibility $\chi^{(1)}$ for the thin films studied was evaluated using the following formula:[63]

$$\chi^{(1)} = \frac{{n_0}^2 - 1'}{4\pi} \tag{11}$$

Furthermore, according to Miller's rule,[64] third-order nonlinear susceptibility ($\chi^{(3)}$) can be evaluated from the linear optical susceptibility ($\chi^{(1)}$) as follows:

$$\chi^{(3)} = A\left(\chi^{(1)}\right)^4 = A\left(\frac{{n_0}^2 - 1'}{4\pi}\right)^4 \tag{12}$$

where, n_0 is the static refractive index for $h\nu \rightarrow 0$ and A is a constant having a value of $\sim 1.7 \times 10^{-10}$ (for $\chi^{(3)}$ measured in esu). The values obtained for linear and nonlinear susceptibility for the irradiated films are shown in Table 3. It was observed that the linear and nonlinear susceptibilities increase monotonically with the ion irradiation doses. The observed nonlinear susceptibility $\chi^{(3)}$ was found to be several orders higher than those of SiO_2 glass ($\chi^{(3)} = 2.8 \times 10^{-14}$ esu), As_2S_3 glass ($\chi^{(3)} = (1.48\text{–}2.2) \times 10^{-14}$ esu), and GeS_2 glass ($\chi^{(3)} = 1 \times 10^{-14}$ esu) which means that the film studied is a promising candidate for optical switching, optical limiting and other nonlinear device applications.[65] Wassel and El Radaf calculated the third order nonlinearities of an $SnS_{1-x}Se_x$ thin film, and observed that the maximum value for SnSe ($x = 1$) film was $\sim 9.412 \times 10^{-12}$ esu, using a theoretical calculation method, whereas the observed nonlinear susceptibility in the film reported here was is 100 times greater than that of the $SnS_{1-x}Se_x$ films.[66] Similarly, Qin *et al.* studied the nonlinear optical characteristics of CdS nanoparticles deposited in a mesoporous silica thin film (MTFs) using a Z-scan technique. The value of nonlinear susceptibility was estimated to be in the range of 7.04×10^{-9} esu which was close to our observed values. The observed nonlinear refractive index (n_2) had a value of 7.83×10^{-18} m^2 W^{-1}.[67] Furthermore, our observed $\chi^{(3)}$ value was also higher than the estimated $\chi^{(3)}$ value (1.73×10^{-13} to 1.09×10^{-11} esu) of the $Cd_{0.99}Zn_{0.01}S$/ZnO nanostructured thin films fabricated on an ITO substrate.[68] The photoinduced effect on the third order nonlinear susceptibility of a nano structured Bi_2Te_3 topological

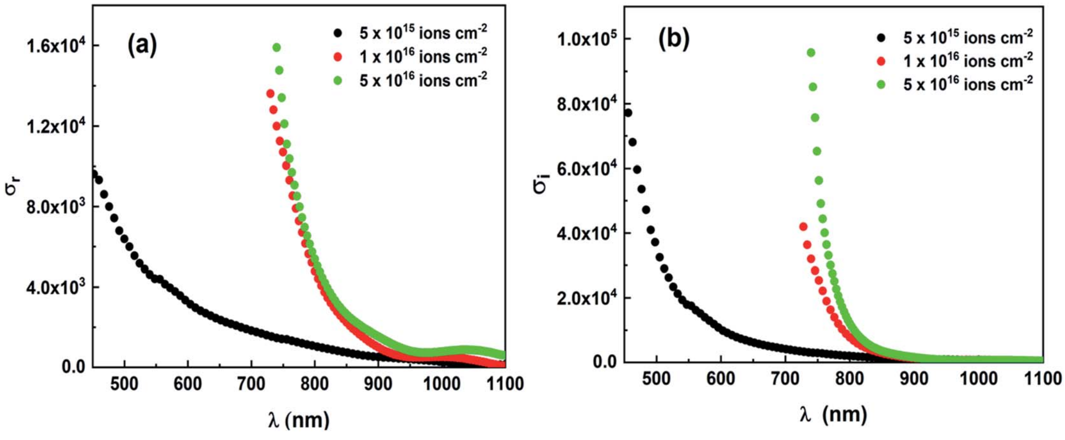

Fig. 11 (a) Real and (b) imaginary optical conductivity plots of the proton irradiated films.

insulator were calculated, and the ellipsometry study showed that the $\chi^{(3)}$ value was 1.23×10^{-10} esu which was of the same order compared to thin film studied here.[69] Chtouki *et al.* studied Ni doped CdS thin films prepared by spin coating on a glass substrate. For this film, the third order nonlinear susceptibilities were calculated using third harmonic generation by the rotational Maker fringe technique and possessed the highest value of $\sim 5.09 \times 10^{-21}$ m^2 V^{-2} for the 2% Ni doped film which was much less when compared to our results.[70]

Finally, the optical nonlinearities observed in this study showed enhanced values for the $Bi_5In_{30}Se_{65}$ film compared to the previously reported data. Several physical phenomena could also be responsible for such observed high nonlinearity, such as the band gap shifting, the presence of highly polarizable Bi, and the presence of lone pair electrons in the chalcogenide Se atoms that can be easily polarized. This resulted in the homogenization and formation of highly polymerized covalent bonds inside the amorphous matrix as a consequence of the ion irradiation.[65]

The behavior of the nonlinear susceptibility and optical bandgap with respect to the ion irradiation doses is shown in Fig. 12. The increase in the nonlinear susceptibility may be due to the enhanced irradiation induced interactions between the fragments which increased the polymerization and homogenization inside the material, that then enhanced the susceptibility.[71]

In addition, the nonlinear refractive index, n_2 of the investigated films were evaluated using Ticha and Tichy, and Miller's rule given by:[72]

$$n_2 = \frac{12\pi\chi^{(3)}}{n_0} \tag{13}$$

The value of the nonlinear refractive index obtained is given in Table 3. The nonlinear refractive index increased with the ion irradiation doses which was due to the increase of irradiation induced defect states that increased the local polarizability.[73] The high value of the nonlinear refractive index indicated that the films studied could be interesting candidates for nonlinear optical applications. The nonlinear optical index, n_2, of Ge_{10}-As_xTe_{90-x} films, observed from an experimental Z-scan technique, showed a maximum index value of 4.96×10^{-13} esu, which was much lower than our observed nonlinear index value.[74] Irradiation of 80 MeV silicon swift heavy ions on a $Ge_{24}Se_{61}Sb_{15}$ thin film resulted in an increase in the n_2 value from 1.7×10^{-10} esu to 2.6×10^{-10} esu, with an increase in ion fluence which also agreed with results in our study.[21] These increases in nonlinear susceptibility and refractive index were due to the polarization dependent nature. The ion irradiation enhanced the polarizability of the material. The tailoring of the nonlinear optical properties of the Bi_2Se_3 film by ion irradiation showed a dependency on the irradiation-induced structural changes, *i.e.*, relative atom displacement (RAD).[75] This irradiation-induced structural modification was observed using Q-switched waveguide laser emission where the Bi_2Se_3 film acted as a passive absorber. In this case, the observed tailoring of the optical nonlinearity was correlated with the bandgap energy and other optical parameters, which can be used for various optical applications.

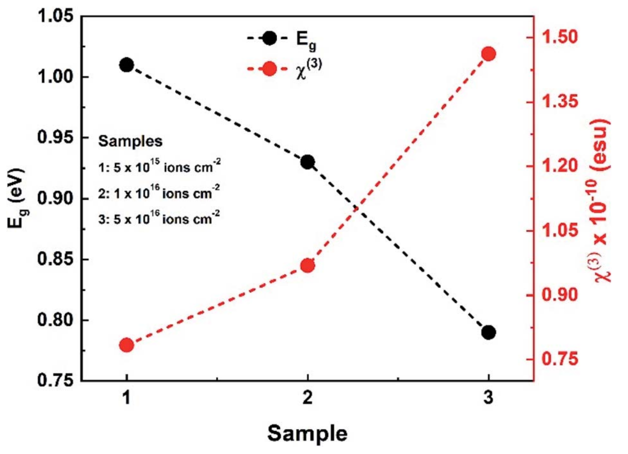

Fig. 12 The variation of $\chi^{(3)}$ and E_g with the ion irradiation dose for the studied thin films.

Optical electronegativity (η_{Opt}). Furthermore, the optical electronegativity, η_{Opt} that represents the ability of the positive radicals of atoms to attract the electrons of the same material to form ionic bonds could be evaluated according to Duffy, by using the static refractive index as follows:[76]

$$\eta_{Opt} = \left(\frac{C}{n_o}\right)^{1/4} \tag{14}$$

where C is a constant having a value of 25.54. The estimated η_{Opt} values are given in Table 3 which shows the reduction in values with ion irradiation doses of the films studied.

4. Conclusions

The study reported here shows the effects of 30 keV proton ion irradiation on $Bi_5In_{30}Se_{65}$ thin films at three different fluences: 5×10^{15} ions per cm^2, 1×10^{16} ions per cm^2, and 5×10^{16} ions per cm^2. The XRD analysis showed the amorphous nature of the irradiated films. The change in surface structure was clearly seen from FESEM and AFM images. The transmittance decreased with irradiation, whereas the absorption coefficient increased with irradiation. The irradiation induced reduction of the optical bandgap with the ion irradiation dose is explained *via* the Mott and Davis model. Increases in the optical density, extinction coefficient, refractive index, real and imaginary dielectric constant, loss factor, VELF, SELF, and skin depth behavior were observed with an increase in the irradiation fluence. The static linear refractive index and high-frequency dielectric constants increased with irradiation. The optical electronegativity decreased with fluence, whereas the real and imaginary parts of the optical conductivity increased with the ion fluence. The third-order nonlinear susceptibility and nonlinear refractive index increased as a consequence, which indicates an increase in polarizability in the local structure. The large nonlinear susceptibility of the material enables it to be a good candidate for use in the manufacture of nonlinear optical devices.

Data availability

The data that support the findings of this study are available from the corresponding author upon reasonable request.

Author contributions

P. Priyadarshini: writing – original draft, software, experiments, data curation, investigation.

S. Das: investigation, experiments.

S. Sahoo: visualization, experiments.

D. Alagarasan: investigation, experiments.

S. Vardharajaperumal: experiments.

R. Ganesan: visualization, investigation.

R. Naik: conceptualization, methodology, writing – review and editing, supervision.

Conflicts of interest

The authors declare that they have no known competing financial interests or personal relationships that could have appeared to influence the work reported in this paper. There are no conflicts of interest relating to this manuscript.

Acknowledgements

R. Naik thanks the Department of Physics, Indian Institute of Science (IISc) for assistance with the optical and FESEM measurements.

References

1 J. A. Frantz, A. Clabeau, J. D. Myers, R. Y. Bekele, V. Q. Nguyen and J. S. Sanghera, *Opt. Express*, 2020, **28**(23), 34744–34753.

2 D. Alagarasan, S. Varadharajaperumal, K. D. A. Kumar, R. Naik, A. Arunkumar and R. Ganesan, Optimization of different temperature annealed nanostructured CdSe thin film for photodetector applications, *Opt. Mater.*, 2021, **122**, 111706.

3 L. Pan, B. Song, N. Mao, C. Xiao, C. Lin and P. Zhang, Optical properties of Ge-Sb-Se thin films induced by femtosecond laser, *Opt. Commun.*, 2021, **496**, 127123.

4 D. Sahoo, P. Priyadarshini, R. Dandela, D. Alagarasan, R. Ganesan, S. Vardharajperumal and R. Naik, In situ laser irradiation: the kinetics of the changes in the nonlinear/linear optical parameters of $As_{50}Se_{40}Sb_{10}$ thin films for photonic applications, *RSC Adv.*, 2021, **11**(26), 16015–16025.

5 P. Sharma, M. Vahistha, V. Ganesan and I. P. Jain, Ion irradiation-induced modifications in the surface morphology of $Ge_{20}Se_{74}Bi_6$ thin films, *J. Alloys Compd.*, 2008, **462**, 452–455.

6 R. Panda, S. A. Khan, U. P. Singh, R. Naik and N. C. Mishra, The impact of fluence dependent 120 MeV Ag swift heavy ion irradiation on the changes in structural, electronic, and optical properties of $AgInSe_2$ nano-crystalline thin films for optoelectronic applications, *RSC Adv.*, 2021, **11**(42), 26218–26227.

7 A. El-Denglawey, V. Sharma, E. Sharma, K. A. Aly, A. Dahshan and P. Sharma, Optical and mechanical properties of Ag doped thermally evaporated SeTe thin films for optoelectronic applications, *J. Phys. Chem. Solids*, 2021, **159**, 110291.

8 M. Behera, R. Naik, C. Sripan, R. Ganesan and N. C. Mishra, Influence of Bi content on linear and nonlinear optical properties of $As_{40}Se_{60-x}Bi_x$ chalcogenide thin films, *Curr. Appl. Phys.*, 2019, **19**, 884–893.

9 S. Pandey and R. Chauhan, Contribution of 80 MeV silicon swift heavy ion irradiation for reforming of optical and structural properties of amorphous $Ge_{23}Se_{62}As_{15}$ thin films for telecommunication and sensing applications, *J. Non-Cryst. Solids*, 2021, **554**, 120597.

10 A. Aparimita, R. Naik, S. Sahoo, C. Sripan and R. Ganesan, Influence of low energy Ag ion irradiation for formation of Bi_2Se_3 phase from Bi/$GeSe_2$ heterostructure thin films, *Appl. Phys. A*, 2020, **126**, 203.

11 G. Goo, G. Anoop, S. Unithrattil, W. S. Kim, H. J. Lee and J. K. Jo, Proton-Irradiation Effects on the Thermoelectric Properties of Flexible Bi_2Te_3/PEDOT: PSS Composite Films, *Adv. Electron. Mater.*, 2019, **5**, 1800786.

12 D. K. Avasthi and G. K. Mehta, *Materials Engineering with Swift Heavy Ions*, Springer Netherlands, 2011.

13 L. Thome, A. Debelle, F. Garrido, S. Mylonas, *et al.*, Radiation effects in nuclear materials: Role of nuclear and electronic energy losses and their synergy, *Nucl. Instrum. Methods Phys. Res., Sect. B*, 2013, **307**, 43–48.

14 Y. Zhang, T. Varga, M. Ishimaru, P. D. Edmondson, H. Xue, P. Liu, S. Moll, F. Namavar, C. Hardiman, S. Shannon and W. J. Weber, Competing effects of electronic and nuclear energy loss on microstructural evolution in ionic-covalent materials, *Nucl. Instrum. Methods Phys. Res., Sect. B*, 2014, **327**, 33–43.

15 S. Jost, F. Hergert, R. Hock, J. Schulze, A. Kirbs, T. Vob and M. Purwins, The formation of $CuInSe_2$ thin film solar cell absorbers from electroplated precursors with varying selenium content, *Sol. Energy Mater. Sol. Cells*, 2007, **91**, 1669–1675.

16 A. Aparimita, M. Behera, C. Sripan, R. Ganesan, S. Jena and R. Naik, Effect of Bi addition on the optical properties of $Ge_{30}Se_{70-x}Bi_x$ thin films, *J. Alloys Compd.*, 2018, **739**, 997.

17 R. K. Pan, H. Z. Tao, H. C. Zang, X. J. Zhao and T. J. Zhang, Optical properties of pulsed laser deposited amorphous $(GeSe_2)_{100-x}Bi_x$ films, *Appl. Phys. A*, 2010, **99**, 889–894.

18 S. Sharma, P. Kumar and R. Thangaraj, Effect of Bi additive on structure and optical properties of amorphous $Bi_xIn_{25-x}Se_{75}$ chalcogenide films, *Curr. Appl. Phys.*, 2013, **13**, 731–735.

19 R. P. Tripathi, M. A. Alvi and S. A. Khan, Investigations of thermal, optical and electrical properties of $Se_{85}In_{15-x}Bi_x$ glasses and thin films, *J. Therm. Anal. Calorim.*, 2020, **146**, 2261–2272.

20 P. Priyadarshini, S. Das, D. Algarasan, R. Ganesan, S. Varadharajaperumal and R. Naik, Role of bismuth

incorporation on the structural and optical properties in $Bi_xIn_{35-x}Se_{65}$ thin films for photonic applications, *J. Am. Ceram. Soc.*, 2021, **104**(11), 5803–5814.

21 S. Pandey and R. Chauhan, Optical and structural modification in amorphous $Ge_{24}Se_{61}Sb_{15}$ thin films under 80 MeV Silicon swift heavy ions for telecom and optical applications, *Opt. Mater.*, 2021, **111**, 110686.

22 P. Sharma, M. Vashistha and P. Jain, Electrical conductivity of ion irradiated $Ge_{20}Se_{80-x}Bi_x$ thin films, *Radiat. Meas.*, 2003, **36**, 663–666.

23 M. Behera, N. C. Mishra and S. A. Khan, Influence of 120 MeV Ag Swift Heavy Ion Irradiation on the optical and electronic properties of As-Se-Bi chalcogenide thin films, *J. Non-Cryst. Solids*, 2020, **544**, 120191.

24 S. K. Tripathi, A. Thakur, G. Singh, J. Sharma, V. Sharma, K. P. Singh, G. S. S. Saini and N. Goyal, Proton-induced changes on the optical parameters of a-$(Ge_{20}Se_{80})_{0.96}Ag_{0.04}$ thin films, *J. Mater. Sci.*, 2006, **41**, 1847–1850.

25 K. V. Kurochka, N. V. Melnikova, D. O. Alikin and T. E. Kurennykh, Irradiation effect on the structural and electrical properties of the glassy Ag-Ge-As-S composite material containing carbon nanotubes, *Solid State Ionics*, 2019, **341**(5), 115026.

26 T. Nichol, G. Nagy, R. Huszank and D. Tenne, Proton beam effects on Ge–Se/Ag thin films, *Phys. Status Solidi B*, 2018, **255**(6), 1700453.

27 B. Koo, J. H. Lee, D. Shin, B. T. Ahn and B. Shin, Photoluminescence study of high energy proton irradiation on Cu $(In,Ga)Se_2$ thin films, *Thin Solid Films*, 2016, **603**, 134–138.

28 S. K. Sahoo, S. Mangal, D. K. Mishra, P. Kumar and U. P. Singh, Effect of low energy proton beam irradiation on structural and electrical properties of ZnO:Al thin films, *Mater. Sci. Semicond. Process.*, 2017, **63**, 76–82.

29 A. V. Krasheninnikov and K. Nordlund, Ion and electron irradiation-induced effects in nanostructured materials, *J. Appl. Phys.*, 2010, **107**, 071301.

30 C. Bo, M. Yang, X. Zheng, W. Li, K. Zhu and S. Priya, Impact of capacitive effect and ion migration on the hysteretic behavior of perovskite solar cells, *J. Phys. Chem. Lett.*, 2015, **6**, 4693–4700.

31 R. M. Hassan, A. Z. Mahmoud, M. A. Abdel-Rahim, H. S. Assaedi, S. W. Alraddadi and A. M. Abd-Elnaiem, Effect of thermal annealing on structure and optical properties of amorphous $As_{30}Te_{64}Ga_6$ thin films, *J. Inorg. Organomet. Polym.*, 2021, **31**, 3037–3053.

32 B. K. Yadav, P. Singh, C. P. Yadav and D. K. Pandey, Synthesis and characterization of $ZnSe_{1-x}Te_x$ thin films, *Phase Transform.*, 2021, **94**, 326–337.

33 S. A. Gad, H. Shaban, B. A. Mansour and G. M. Mahmoud, Determination and analysis of linear and nonlinear optical properties and electrical conductivity of amorphous $Pb_xGe_{42-x}Se_{48}Te_{10}$ thin films, *Appl. Phys. A: Mater. Sci. Process.*, 2020, **26**, 354.

34 E. R. Shaaban, Y. A. M. Ismail and H. S. Hassan, Compositional dependence of the optical properties of amorphous $Se_{80-x}Te_{20}Bi_x$ thin films using transmittance and reflectance measurements, *J. Non-Cryst. Solids*, 2013, **376**, 61–67.

35 R. Naik, C. Sripan and R. Ganesan, Photo darkening in $As_{50}Se_{50}$ thin films by 532 nm laser irradiation, *Opt. Laser Technol.*, 2017, **90**, 158–164.

36 M. R. Balboul, Optical effects induced by gamma and UV irradiation in chalcogenide glass, *Radiat. Meas.*, 2008, **43**, 1360–1364.

37 A. A. A. Darwish, M. Rashad, A. E. Bekheet and M. M. El-Nahass, Linear and nonlinear optical properties of $GeSe_{2-x}Sn_x$ $(0 \le x \le 0.8)$ thin films for optoelectronic applications, *J. Alloys Compd.*, 2017, **709**, 640–645.

38 J. Tauc, *Amorphous and Liquid Semiconductors*, Plenum Press, New York, 1979.

39 P. Priyadarshini, S. Das, D. Alagarasan, R. Ganesan, S. Vardharajperumal and R. Naik, Observation of high nonlinearity in Bi doped $Bi_xIn_{35-x}Se_{65}$ thin films with annealing, *Sci. Rep.*, 2021, **11**, 21518.

40 K. Senthil, D. Mangalaraj, S. K. Narayandass, B. Hong, Y. Roh, C. S. Park and J. Yi, Argon and nitrogen implantation effects on the structural and optical properties of vacuum evaporated cadmium sulphide thin films, *Semicond. Sci. Technol.*, 2002, **17**, 97.

41 N. F. Mott and E. A. Davis, *Electronics Processes in Non-crystalline Materials*, Clarendon, Oxford, 1979, p. 428.

42 G. A. Amin, S. M. El-Sayed, H. M. Saad, F. M. Hafez and M. Abd-El-Rahman, The radiation effect on optical and morphological properties of Ag–As–Te thin films, *Radiat. Meas.*, 2007, **42**, 400–406.

43 X. Xhang, Y. Liu, H. Lei and B. Li, An organic–inorganic broadband photodetector based on a single polyaniline nanowire doped with quantum dots, *Nanoscale*, 2016, **8**, 15529–15537.

44 X. Yang, L. Wah, J. Yan, Y. Bao, Q. Chen, A. Camposeo, D. Pisignano and B. Li, Energy dissipation and asymmetric excitation in hybrid waveguides for routing and coloring, *J. Phys. Chem. Lett.*, 2021, **12**, 7034–7040.

45 Q. Li, H. Rao, X. Ma, H. Mei, Z. Zhao, W. Gong, A. Camposeo, D. Pisignano and X. Yang, Unusual redlight emission from non-metallic Cu_2Te microdisk for laser and SERS applications, *Adv. Opt. Mater.*, 2022, **10**, 2101976.

46 S. N. Moger and M. G. Mahesha, Colour tunable co-evaporated CdS_xSe_{1-x} $(0 \le x \le 1)$ ternary chalcogenide thin films for photodetector applications, *Mater. Sci. Semicond. Process.*, 2020, **120**, 105288.

47 X. Yang and B. Li, Monolayer MoS_2 for nanoscale photonics, *Nanophotonics*, 2020, **9**, 1557–1577.

48 V. Dadi and S. Peravali, Structural and optical analysis of film $Sn_{6.3}Pb_{93.7}$ prepared from coarse $Sn_{63}Pb_{37}$, *Opt. Mater.*, 2022, **123**, 111908.

49 S. Yasmeen, F. Iqbal, T. Munawar, M. A. Nawaz, M. Asghar and A. Hussain, Synthesis, structural and optical analysis of surfactant assisted ZnO–NiO nanocomposites prepared by homogeneous precipitation method, *Ceram. Int.*, 2019, **45**, 17859–17873.

50 T. S. Moss, Proceedings of the physical society, Section B, a relationship between the refractive index and the infra-

red threshold of sensitivity for photoconductors, *Proc. Phys. Soc., London, Sect. B*, 1950, **63**, 167–175.

51 R. Naik, S. Jena, R. Ganesan and N. K. Sahoo, Photo-induced optical bleaching in $Ge_{12}Sb_{25}S_{63}$ amorphous chalcogenide thin films: effect of 532 nm laser illumination, *Laser Phys.*, 2015, **25**(3), 036001.

52 A. A. Attia, M. M. El-Nahass, M. Y. El-Bakry and D. M. Habashy, Neural networks modelling for refractive indices of semiconductors, *Opt. Commun.*, 2013, **287**, 140–144.

53 V. Dimitrov and S. Sakka, Linear and non-linear optical properties of simple oxides, *J. Appl. Phys.*, 1996, **79**, 1741–1745.

54 A. S. Hassanien, K. A. Aly and A. A. Akl, Study of optical properties of thermally evaporated ZnSe thin films annealed at different pulsed laser powers, *J. Alloys Compd.*, 2016, **685**, 733–742.

55 K. Sharma, A. S. Al-Kabbi, G. S. S. Saini and S. K. Tripathi, Determination of dispersive optical constants of nanocrystalline CdSe (nc-CdSe) thin films, *Mater. Res. Bull.*, 2012, **47**, 1400.

56 A. S. Hassanien and I. Sharma, Optical properties of quaternary a-$Ge_{15-x}Sb_xSe_{50}Te_{35}$ thermally evaporated thin-films: refractive index dispersion and single oscillator parameters, *Optik*, 2020, **200**, 163415.

57 N. F. Habui, S. F. Oboudi and S. S. Chiad, Study of some optical properties of mixed SnO_2-CuO thin films, *J. Nano-Electron. Phys.*, 2012, **4**, 4008–4012.

58 X. Zhang, F. Chen, R. Lin, Y. Huang, S. Dai, Q. Nie, X. Zhang and W. Ji, Investigation of third-order optical nonlinearities of copper doped germanium-gallium-sulfur chalcogenide glasses, *J. Non-Cryst. Solids*, 2017, **475**, 167–171.

59 H. E. Atyia and N. A. Hegab, Determination and analysis of optical constants for $Ge_{15}Se_{60}Bi_{25}$ thin films, *Phys. B*, 2016, **454**, 189–196.

60 S. Sarkar, N. S. Das and K. K. Chattopadhyay, Optical constants, dispersion energy parameters and dielectric properties of ultra-smooth nanocrystalline $BiVO_4$ thin films prepared by rf-magnetron sputtering, *Solid State Sci.*, 2014, **33**, 58–66.

61 S. S. Fouad, I. M. El Radaf, P. Sharma and M. S. El-Bana, Multifunctional CZTS thin films: Structural, optoelectrical, electrical and photovoltaic properties, *J. Alloys Compd.*, 2018, **757**, 124–133.

62 A. A. M. Farag, A. Ashery and M. A. Shenashen, Optical absorption and spectrophotometric studies on the optical constants and dielectric of poly(*o*-toluidine) (POT) films grown by spin coating deposition, *Phys. B*, 2012, **407**, 2404–2411.

63 S. Mishra, P. K. Singh, R. K. Yadav, R. K. Yadav, A. Umar, P. Lohia and D. K. Dwivedi, Investigation of glass forming ability, linear and non-linear optical properties of Ge-Se-Te-Sb thin films, *Chem. Phys.*, 2021, **541**, 111021.

64 J. J. Wynne, Optical third-order mixing in GaAs, Ge, Si, and InAs, *Phys. Rev.*, 1969, **178**, 129.

65 M. Frumar, J. Jaselsky, B. Frumarova, T. Wagner and M. Hrdlicka, Optically and thermally induced changes of structure, linear and non-linear optical properties of chalcogenides thin films, *J. Non-Cryst. Solids*, 2003, **326–327**, 399–404.

66 A. R. Wassel and I. M. El Radaf, Synthesis and characterization of the chemically deposited $SnS_{1-x}Se_x$ thin films: structural, linear and nonlinear optical properties, *Appl. Phys. A*, 2020, **126**, 177.

67 F. Qin, J. L. Shi and J. L. Gu, Large incorporation amount and enhanced nonlinear optical properties of sulfide nanoparticles within mesoporous thin films, *J. Mater. Chem.*, 2008, **18**, 634–636.

68 Z. R. Khan, A. S. Alshammari, M. Shkir and S. AlFaify, Linear, third order nonlinear optical and photoluminescence properties of $Cd_{0.\ 99}Zn_{0.\ 09}S$/ZnO nanocomposite thin films for optoelectronics applications, *Surf. Interfaces*, 2020, **20**, 100561.

69 E. A. H. Aviles, M. T. Valdez, J. A. Torres, C. J. Ramos Torroes, H. M. Guteierrez and C. Torres-Torres, Photo-induced structured waves by nanostructured topological insulator Bi_2Te_3, *Opt. Laser Technol.*, 2021, **140**, 107015.

70 T. Chtouki, Y. El Kouari, B. Kulyk, A. Louardi, A. Rmili, H. Erguig, B. Elidrissi, L. Soumahoro and B. Sahraoui, Spin-coated nickel doped cadmium sulfide thin films for third harmonic generation applications, *J. Alloys Compd.*, 2017, **696**, 1292–1297.

71 D. Sahoo, P. Priyadarshini, A. Aparimita, D. Alagarasan, R. Ganesan, S. Varadharajaperumal and R. Naik, Optimization of linear and nonlinear optical parameters of $As_{40}Se_{50}Te_{10}$ thin films by thermal annealing, *Opt. Laser Technol.*, 2021, **140**, 107036.

72 H. Ticha and L. Tichy, Semiempirical relation between non-linear susceptibility (refractive index), linear refractive index and optical gap and its application to amorphous chalcogenides, *J. Optoelectron. Adv. Mater.*, 2002, **4**, 381–386.

73 A. A. A. Darwish and H. A. M. Ali, On annealing induced effect in optical properties of amorphous GeSeSn chalcogenide films for optoelectronic applications, *J. Alloys Compd.*, 2017, **710**, 431–435.

74 Q. Li, R. Wang, F. Xu, X. Wang, Z. Yang and X. Gai, Third-order nonlinear optical properties of Ge-As-Te chalcogenide glasses in mid-infrared, *Opt. Mater. Express*, 2020, **10**, 1413–1420.

75 Y. Tan, Z. Guo, Z. Shang, *et al.*, Tailoring nonlinear optical properties of Bi_2Se_3 through ion irradiation, *Sci. Rep.*, 2016, **6**, 21799.

76 J. A. Duffy, Trends in energy gaps of binary compounds: an approach based upon electron transfer parameters from optical spectroscopy, *J. Phys. C: Solid State Phys.*, 1980, **13**, 2979–2989.